

# A 4×256 Gbps silicon transmitter with on-chip adaptive dispersion compensation

Received: 8 November 2024

Accepted: 18 June 2025

Published online: 07 July 2025

 Check for updates

Shihuan Ran<sup>1</sup>, Yu Guo<sup>1</sup>, Yuanbin Liu<sup>1</sup>, Ting Miao<sup>1</sup>, Yangbo Wu<sup>2</sup>, Yang Qin<sup>2</sup>, Yuyao Guo<sup>1,3</sup>, Liangjun Lu<sup>1,3</sup>, Yixiao Zhu<sup>1</sup>, Yu Li<sup>1,3</sup>✉, Qunbi Zhuge<sup>1</sup>✉, Jianping Chen<sup>1,3</sup> & Linjie Zhou<sup>1,3</sup>

The exponential growth of data traffic propelled by cloud computing and artificial intelligence necessitates advanced optical interconnect solutions. While wavelength division multiplexing (WDM) enhances optical module transmission capacity, chromatic dispersion becomes a critical limitation as single-lane rates exceed 200 Gbps. Here we demonstrate a 4-channel silicon transmitter achieving 1 Tbps aggregate data rate through integrated adaptive dispersion compensation. This transmitter utilizes Mach-Zehnder modulators with adjustable input intensity splitting ratios, enabling precise control over the chirp magnitude and sign to counteract specific dispersion. At 1271 nm (−3.99 ps/nm/km), the proposed transmitter enabled 4 × 256 Gbps transmission over 5 km fiber, achieving bit error ratio below both the soft-decision forward-error correction threshold with feed-forward equalization (FFE) alone and the hard-decision forward-error correction threshold when combining FFE with maximum-likelihood sequence detection. Our results highlight a significant leap towards scalable, energy-efficient, and high-capacity optical interconnects, underscoring its potential in future local area network WDM applications.

The rapid proliferation of cloud computing, artificial intelligence (AI), 5 G networks, and the Internet of Things (IoT) has led to an unprecedented surge in data traffic within data centers<sup>1–3</sup>. This exponential growth demands significant advancements in optical communication technologies to enhance both data transmission rates and energy efficiency. High-speed optical modules operating in the O-band are typically employed in data centers due to minimal chromatic dispersion in this wavelength range, utilizing intensity modulation direct detection (IM-DD) schemes. To further increase communication capacity, wavelength division multiplexing (WDM) has been adopted, allowing multiple wavelengths to carry data simultaneously and thus achieving higher aggregate transmission rates<sup>4–6</sup>. However, as WDM systems utilize wavelengths that deviate from the zero-dispersion wavelength (approximately 1310 nm), chromatic dispersion in standard single-mode fibers becomes increasingly significant. For instance,

at 1271 nm, the dispersion value ranges from −2.36 to −4.96 ps/nm/km<sup>7</sup>. This dispersion can severely limit transmission distance and data integrity, especially at data rates exceeding 200 Gbps where signal bandwidths are substantially broader<sup>8–11</sup>.

Limited by the fiber dispersion, the typical transmission distance at the edge wavelength of 1271 nm is only 6 km in the 400GBASE-LR4-6 application<sup>6</sup>, and the distance is further reduced to less than 2 km in the 800GBASE-FR application<sup>12</sup>. In the current development of future IEEE 802.3dj standard, local area network WDM (LAN-WDM) wavelengths with low dispersion are employed for 800GBASE-LR applications with a transmission distance of 10 km, designated to reduce the impact of fiber dispersion<sup>13</sup>. However, it is anticipated that the limited transmission channels within the low-dispersion wavelength range will soon be insufficient to accommodate the escalating demand for communication capacity. Therefore, to further enhance overall

<sup>1</sup>State Key Laboratory of Photonics and Communications, School of Information Science and Electronic Engineering, Shanghai Jiao Tong University, Shanghai 200240, China. <sup>2</sup>Huawei Technologies, Wireless BU, Shanghai 201206, China. <sup>3</sup>SJTU-Pinghu Institute of Intelligent Optoelectronics, Pinghu 314200, China.

✉ e-mail: [yuli\\_seiee@sjtu.edu.cn](mailto:yuli_seiee@sjtu.edu.cn); [qunbi.zhuge@sjtu.edu.cn](mailto:qunbi.zhuge@sjtu.edu.cn)

transmission capacity, it's critical to expand the operating wavelength range beyond the low-dispersion region in WDM applications. While coherent communication systems are able to achieve complete fiber dispersion compensation via digital signal processing (DSP) schemes at the expense of increased system cost, power consumption, and latency, IM-DD systems face fundamental limitations in DSP-based full dispersion mitigation due to the absence of signal phase information<sup>14</sup>. Although advanced DSP algorithms like maximum likelihood sequence detection (MLSD) have been implemented to address dispersion-induced inter-symbol interference (ISI), the effectiveness of such mitigation remains constrained<sup>15–18</sup>. Experimental measurements demonstrate that a 176 Gbps four-level pulse amplitude modulation (PAM-4) signal transmitted through 34 ps/nm dispersion fiber exhibits ~3 dB power penalty at the 20% soft-decision forward-error correction (SD-FEC) threshold, even with MLSD-enabled receivers<sup>16</sup>. Broadcom's simulation analyses further indicate that for a 225 Gbps PAM-4 signal propagating through 13.4 ps/nm dispersion fiber, the transmitter dispersion eye closure quaternary (TDECQ) metric increases dramatically from 1.42 dB to 13.2 dB under MLSD reception, far exceeding the 3.4 dB threshold specified in IEEE 802.3 standard<sup>6,17</sup>. Additionally, the quadratic dependence of dispersion-induced power penalty on baud rate poses escalating challenges in WDM systems, particularly as data rates increase and chromatic dispersion magnifies at edge operating wavelengths<sup>18,19</sup>. These technical constraints necessitate on-chip optical-domain dispersion compensation strategies to effectively minimize bit error ratio (BER) post-transmission and extend viable transmission distances in high-speed IM-DD systems. Furthermore, on-chip optical-domain dispersion compensation demonstrates superior advantages over DSP-based approaches, notably in reduced power consumption, minimized latency, and alleviated implementation complexity<sup>20–27</sup>. Regular on-chip integrated dispersion compensation schemes include cascaded Mach-Zehnder interferometers (MZIs)<sup>28,29</sup>, waveguide Bragg gratings<sup>30–32</sup>, and cascaded all-pass micro-ring resonators (MRRs)<sup>33,34</sup>. However, these on-chip dispersion compensation schemes have thus far only been verified at the device level and have not yet been demonstrated in combination with on-chip modulators.

In this work, we introduce a 4-channel silicon photonic transmitter with integrated on-chip adaptive dispersion compensation designed to overcome these limitations. The transmitter employs silicon Mach-Zehnder modulators (MZMs) equipped with adjustable input intensity splitting ratio tuners. By dynamically controlling the input light intensity between the two arms of the MZM, we can precisely manipulate the chirp magnitude and sign of the modulated signals. This adaptive chirp control enables effective compensation for varying fiber dispersion across different WDM wavelengths, without the need for additional power-consuming components. For a proof-of-concept demonstration, we validate the transmitter's adaptive dispersion compensation performance at the high-dispersion wavelength of 1271 nm. We successfully transmit  $4 \times 256$  Gbps and  $4 \times 200$  Gbps PAM-4 signals over 5 km and 10 km of standard single-mode fiber, respectively. The achieved BER is below the 6.7% hard-decision forward-error correction (HD-FEC) threshold<sup>35</sup>, all without resorting to pre-emphasis techniques. Our results represent a significant advancement in silicon photonic transmitters, highlighting their potential for scalable, energy-efficient, and high-capacity optical interconnects in future data centers and high-performance computing applications.

## Results

### Device structure and theoretical analysis

Figure 1a depicts the schematic diagram of a 4-channel dispersion compensation-enabled transmitter, consisting of MZMs with a configurable input intensity splitting ratio tuner. The de-interleaver allocates the input multi-wavelength optical source to the corresponding modulation channel. The interleaver is subsequently employed to perform wavelength multiplexing, allowing signals to be transmitted through a

single optical fiber. A  $1 \times 2$  thermal-optic MZI functions as an intensity tuner to adjust the input light intensity of MZM's two branches.

For the MZM integrated with an input intensity tuner, the optical fields at the input and output of the MZM are denoted as  $E_i$  and  $E_o$ , respectively. The optical input intensity splitting ratio for the upper and lower arms is defined as  $A^2 : B^2$ , where  $A^2 + B^2 = 1$ , with associated optical field loss factors  $\alpha_1$  and  $\alpha_2$ , respectively. The output optical field  $E_o$  can then be expressed as:

$$E_o = \alpha_1 A E_i e^{j\theta_A} + \alpha_2 B E_i e^{j\theta_B} \quad (1)$$

where  $\theta_A$  and  $\theta_B$  represent the optical phase shifts in the upper and lower arms, respectively.

For a push-pull drive silicon MZM,  $\theta_A$  and  $\theta_B$  can be expressed as:

$$\theta_A = \theta_h + \theta_{dc} - \theta_{rf} \quad (2)$$

$$\theta_B = \theta_{dc} + \theta_{rf} \quad (3)$$

where,  $\theta_h = \pm \pi/2$  represents the relative optical phase shift between the two arms induced by the heater, positioning the MZM to operate at the quadrature point;  $\theta_{dc}$  denotes the optical phase shift caused by the reverse bias voltage of the PN junction, which remains constant with fixed bias voltage.  $\theta_{rf}$  corresponds to the optical phase shift resulting from the modulation signal.

Let  $A = B \pm \Delta B$ , where  $\Delta B$  is the difference in optical field between the two arms. Under the assumption that  $\alpha_1 = \alpha_2$ , and accounting for the push-pull drive configuration of the MZM, Eq. (1) becomes (as detailed in Supplementary Information 2):

$$E_o = \underbrace{\pm \alpha_1 \Delta B E_i e^{j\theta_h} e^{j\theta_{dc}} e^{-j\theta_{rf}}}_{\text{Phase modulation}} + \underbrace{2\alpha_1 B E_i \cos\left(\frac{\theta_h - 2\theta_{rf}}{2}\right) e^{j\frac{\theta_h + 2\theta_{dc}}{2}}}_{\text{Amplitude modulation}} \quad (4)$$

According to Eq. (4), when the optical power in the two arms of the MZM is identical, i.e.,  $A = B$  and  $\Delta B = 0$ , the coefficient of the first term in Eq. (4) becomes zero. Under these conditions, with  $\theta_h$  and  $\theta_{dc}$  being constants, the phase of the modulation signal in the second term, given by  $(\theta_h + 2\theta_{dc})/2$ , remains unchanged. Consequently, the modulated signal exhibits pure amplitude modulation with an instantaneous frequency shift of zero. Thereby transmitted signal possesses a fixed instantaneous frequency and exhibits no chirp. In contrast, when the optical power in the two arms of the MZM is unequal, i.e.,  $A \neq B$  and  $\Delta B \neq 0$ , the presence of the first term in Eq. (4) leads to residual phase modulation. As a result, an instantaneous frequency shift occurs, thereby endowing the modulated signal with a chirp effect. Specifically, the chirp occurs exclusively during transitions between different signal levels and can be described as a transient chirp<sup>36,37</sup>. Overall, the generation of chirp is attributed to the combined interaction between the MZI, which induces optical power imbalance, and the MZM for signal modulation.

The chirp  $\alpha$ -parameter of the modulated signal is (see Supplementary Information 2 for details)<sup>38–40</sup>:

$$\alpha = 2I_o \frac{d\vartheta/dt}{dI_o/dt} = 2I_o \frac{2\pi\Delta f}{dI_o/dt} = \pm \frac{\alpha_2^2 B^2 - \alpha_1^2 A^2}{2\alpha_1 \alpha_2 AB} \quad (5)$$

where  $I_o$  and  $\vartheta$  denote the optical intensity and phase of the modulated signal, respectively.  $\Delta f = (d\vartheta/dt)/2\pi$  represents the instantaneous frequency shift of the modulation signal. The symbols + and – correspond to the case where  $\theta_h = +\pi/2$  and  $\theta_h = -\pi/2$ , respectively. Notably, it is important to observe that the chirp sign can be reversed either by swapping the splitting ratio between the two arms or by adjusting the relative optical phase shift  $\theta_h$  induced between the two arms through the TiN heater. Upon precise control of the intensity tuner, a matched

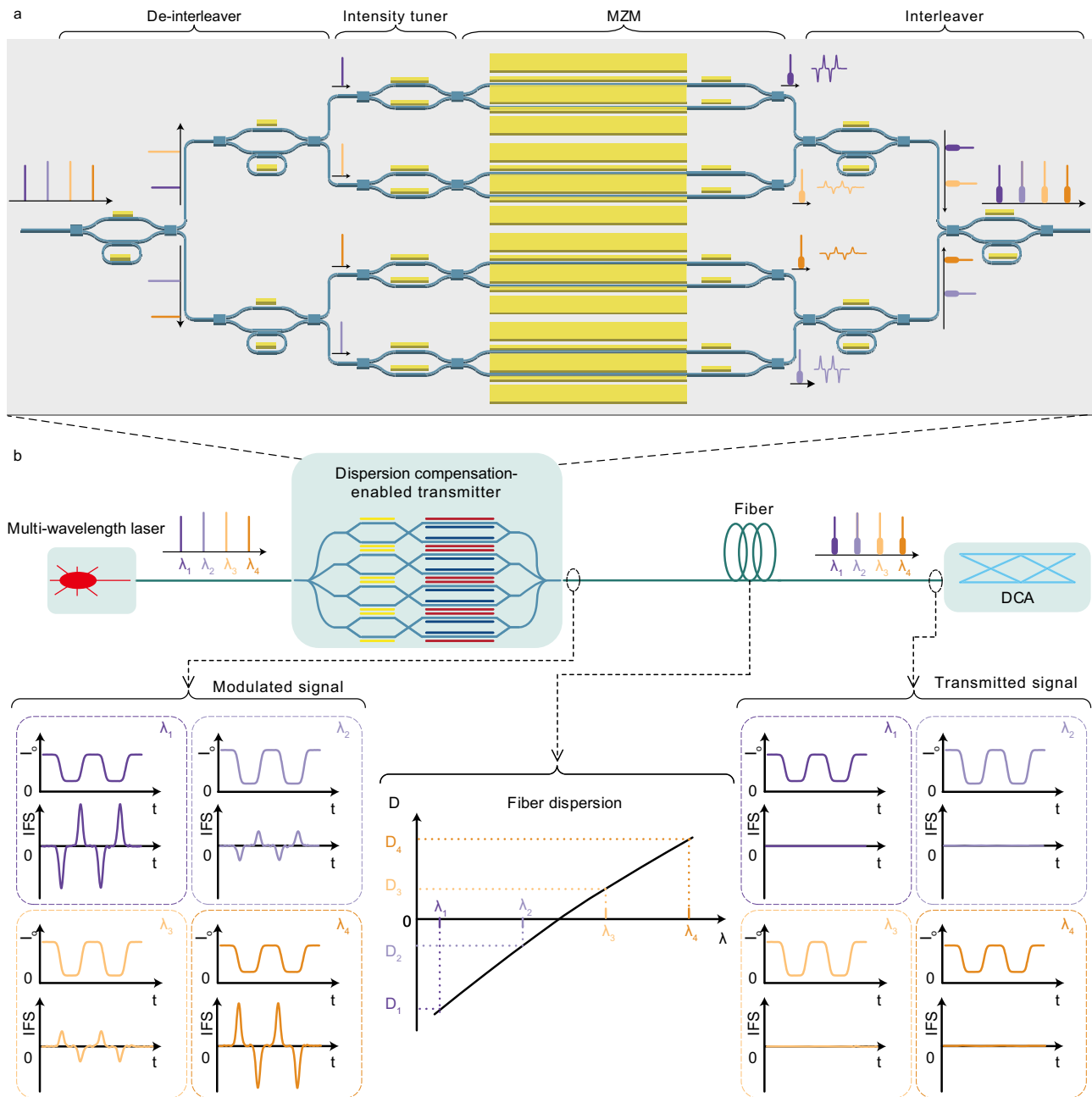


**Fig. 1 | Schematic diagram and working principle of the dispersion compensation-enabled transmitter.** **a** A 4-channel transmitter composed of (de) interleavers and MZMs with configurable input intensity tuners. MZM Mach-Zehnder

modulator. **b** Working principle of the dispersion compensation-enabled transmitter.  $I_o$ , optical intensity,  $t$  time, IFS instantaneous frequency shift,  $D$  dispersion coefficient, DCA digital communication analyzer.

negative (positive) chirp to the modulation signal is generated and aligned with the corresponding positive (negative) fiber dispersion at the operating wavelength, enabling dispersion compensation for the IM-DD transmission link, as illustrated in Fig. 1b. For wavelengths  $\lambda_1$  and  $\lambda_2$ , which exhibit varying negative dispersion coefficients, the intensity tuner can be fine-tuned to generate positive chirp signals with variable amplitudes, thereby effectively compensating for the varying negative dispersion. According to Eq. (5), for positively chirped signals, during the rising (falling) edge of the optical intensity, the instantaneous frequency shift is positive (negative), as the modulated signal shown in Fig. 1b. Conversely, for wavelengths  $\lambda_3$  and  $\lambda_4$ , characterized by varying positive dispersion coefficients, the intensity tuner can be adjusted to produce negative chirp signals with designated amplitudes, effectively mitigating the positive dispersion. Similarly, for negatively chirped signals, during the rising (falling) edge of the optical intensity, the instantaneous

frequency shift is negative (positive). Notably, the amplitude of the chirp can be quantitatively represented by the magnitude of the instantaneous frequency shift. After fiber transmission, the instantaneous frequency shift of the signals at all four wavelengths is zero under perfect chromatic dispersion compensation, as the transmitted signal shown in Fig. 1b.

Considering the effects of fiber dispersion, the Fourier transform of the transmitted optical signal can be expressed as (see Supplementary Information 2 for details):

$$I'_o(\omega) = \mathcal{F}\{I'_o\} = \pm 4\alpha_1\alpha_2ABI_i\theta_{rf}(\omega) \cos\left(\frac{\omega^2\beta L}{2}\right) + 2(\alpha_1^2A^2 - \alpha_2^2B^2)I_i\theta_{rf}(\omega) \sin\left(\frac{\omega^2\beta L}{2}\right) \quad (6)$$

where  $I_i$  is the MZM's input optical intensity,  $\omega$  is the angular frequency of the microwave signal,  $\beta$  and  $L$  are the group velocity dispersion

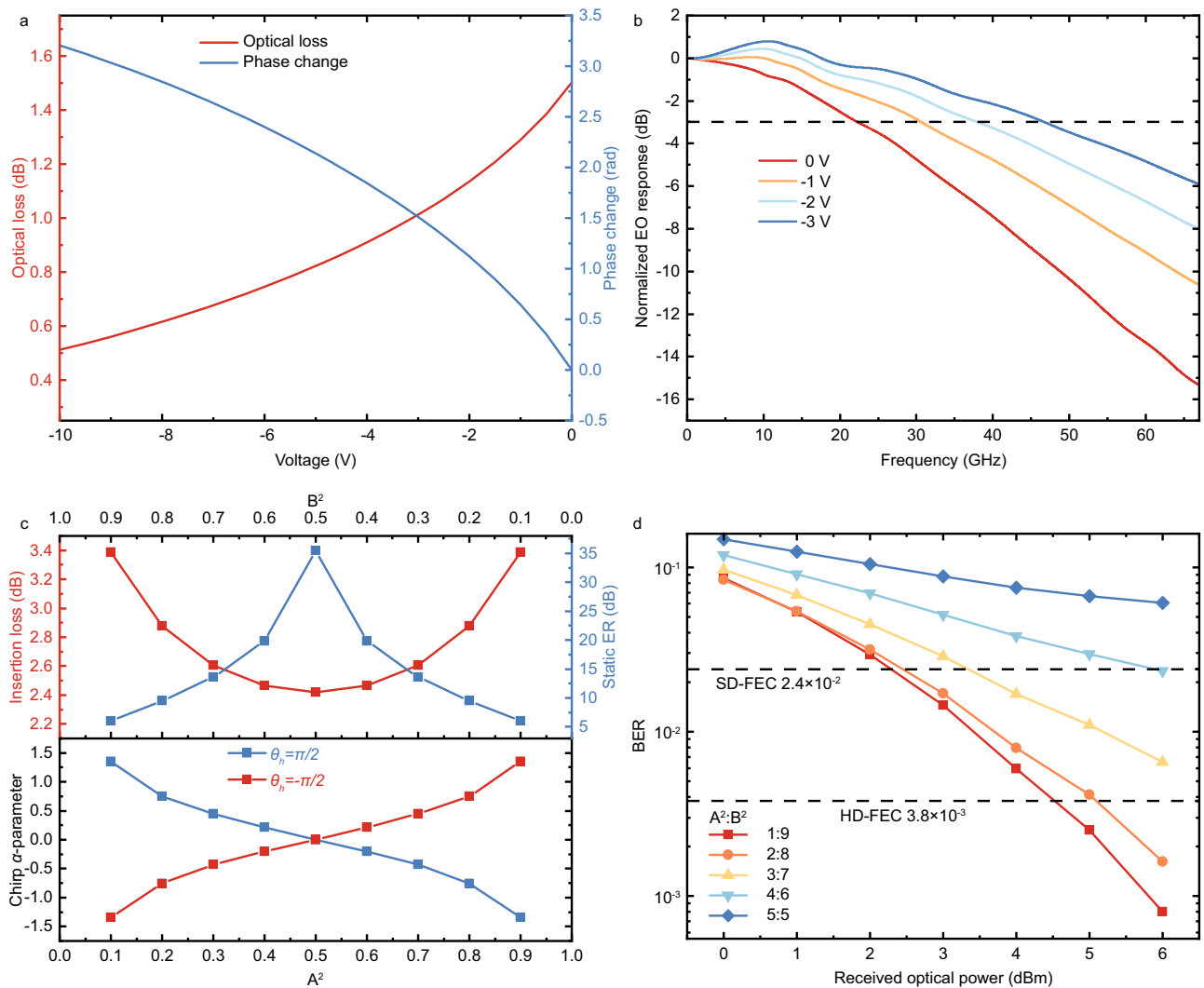


**Fig. 2 | The transmitter's simulation results. a** Simulated optical loss and phase change of the high-speed EO phase shifter. **b** Simulated EO response of the MZM at various bias voltages. **c** Simulated insertion loss, static ER, and small-signal chirp

$\alpha$ -parameter of the MZM. **d** Simulated bit error ratio of the proposed MZM after 5 km fiber transmission upon 256 Gbps PAM-4 modulation.

parameter and length of the fiber, respectively. Note that, when  $\alpha_1^2 A^2 = \alpha_2^2 B^2$ , the second term in Eq. (6) becomes zero. In this case, the remaining cosine function, influenced by fiber dispersion, leads to the power fading of the transmitted signal. Conversely, when  $\alpha_1^2 A^2 \neq \alpha_2^2 B^2$ , the presence of a sine function in the second term alleviates the power-fading effect. Furthermore, with an increase in  $|\alpha_1^2 A^2 - \alpha_2^2 B^2|$ , the amplitude of the sine function rises correspondingly, leading to an enhanced dispersion compensation effect. Therefore, the integration of adaptive input intensity tuners enables MZMs to mitigate signal degradation caused by fiber dispersion.

### Simulation results

To numerically evaluate the performance of the proposed design, we conducted a comprehensive series of simulations, as displayed in Fig. 2. The parameters of the simulation were chosen to be consistent with the experimental setup described in Supplementary Information 1. For MZMs with a 2.5 mm-long phase shifter, an optical loss of -1.5 dB is attained at 0 V using finite difference eigenmode simulations (Lumerical), as shown in Fig. 2a. In addition, the simulated MZM exhibits a modulation efficiency of 2.38 V-cm and an EO bandwidth of -46.5 GHz (Fig. 2b).

Next, we characterize the small-signal chirp  $\alpha$ -parameter of the MZM when an adaptive input intensity tuner is employed, as shown in Fig. 2c. As the intensity disparity between the two arms increases, the absolute value of the chirp  $\alpha$ -parameter rises, enhancing the modulated signal's resilience to fiber dispersion. Specifically, for the scenario where  $\theta_h = \pi/2$ , the chirp  $\alpha$ -parameter is positive when  $A^2$  is less than  $B^2$ , negative when  $A^2$  exceeds  $B^2$ , and nearly zero when  $A^2$  equals  $B^2$ . Conversely, in the scenario where  $\theta_h = -\pi/2$ , the chirp amplitude remains consistent across various splitting ratios, while the chirp sign is inverted. In extreme cases where  $A^2:B^2 = 1:9$  or  $9:1$ , the chirp  $\alpha$ -parameter attains an absolute value of  $\sim 1.3$ , with an extra insertion loss of -1 dB for the MZM due to the imbalanced splitting ratio. Note that, this additional insertion loss does not affect the average optical power of the modulated signal, as the MZM operates at the quadrature point. Meanwhile, the static extinction ratio (ER) of the MZM also decreases as the difference in input light intensity between the two arms increases. Specifically, the static ER drops from 35 dB to 6 dB as the  $A^2:B^2$  ratio transitions from 5:5 to 1:9. Although a larger chirp  $\alpha$ -parameter can be obtained by further increasing the ratio, the reduction in static ER will lead to a corresponding decrease in the dynamic ER of the modulation signal, resulting in signal degradation.

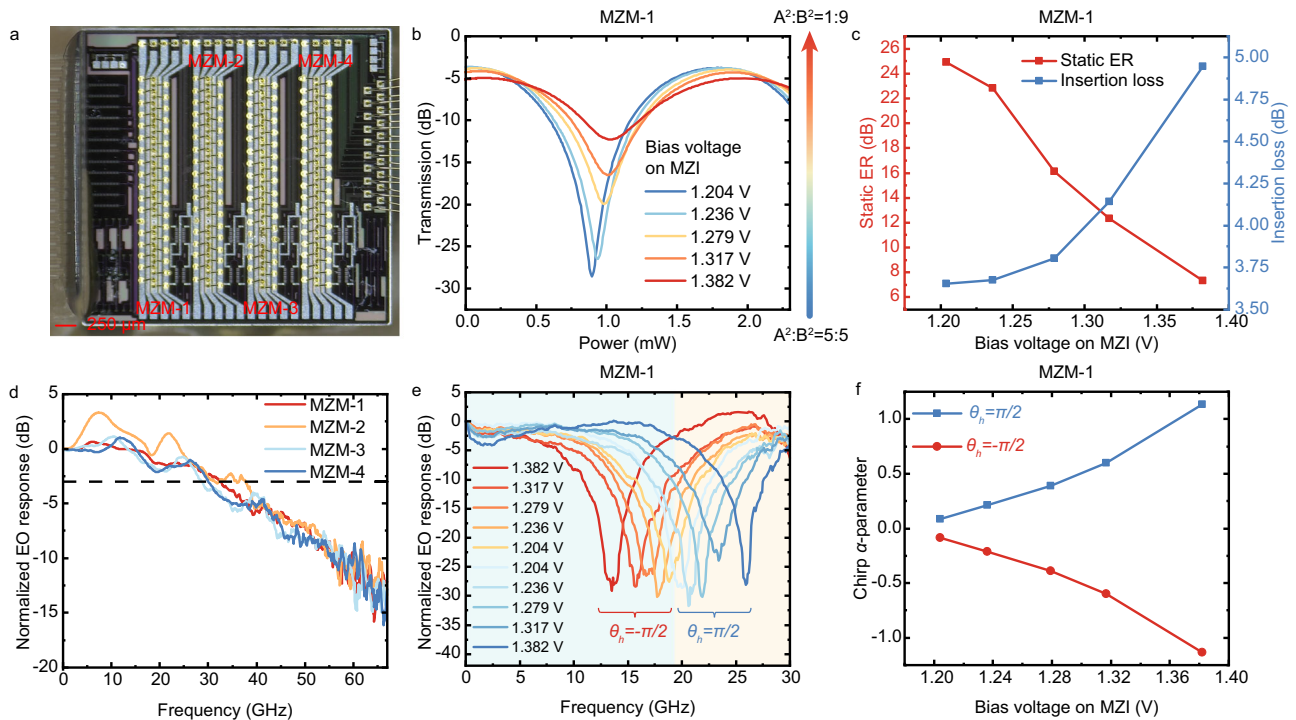


**Fig. 3 | The transmitter's microscope image and experimental results.**

**a** Microscope image of the manufactured silicon transmitter. **b** Measured transmission of the MZM-1 versus electrical power on MZM-1's heater at various bias voltages on MZI. **c** Extracted insertion loss and static ER of MZM-1 at various bias voltages on MZI. **d** Measured normalized EO response of the MZMs at -2 V bias

voltage when  $A^2 \approx B^2$ . **e, f** Measured normalized EO response (**e**) and the extracted chirp  $\alpha$ -parameters (**f**) of the MZM-1 upon -2 V bias voltage at 1271 nm after 50 km standard G652.D type fiber transmission, with various bias voltage applied to the MZI.

Finally, to explore the transmission capability of the MZM, we simulate the BER of a 256 Gbps PAM-4 signal following a 5 km fiber transmission. The 1271 nm wavelength, which exhibits a dispersion of  $-3.99$  ps/nm/km, is chosen to assess the scheme's dispersion compensation performance since it is typically employed as the starting wavelength of the WDM systems at O-band<sup>41,42</sup>. When  $A^2:B^2 = 5:5$ , the recorded BER is larger than the 20% SD-FEC threshold of  $2.4 \times 10^{-2}$ . Increasing  $A^2:B^2$  to 4:6, the BER is improved to marginally below the 20% SD-FEC threshold at 6 dBm input optical power. Further adjusting  $A^2:B^2$  to beyond 2:8 achieves reduced BERs below the 6.7% HD-FEC threshold of  $3.8 \times 10^{-3}$ . The gradual reduction in BER upon increased splitting ratio deviation effectively validates the adaptability of the proposed dispersion compensation scheme. In particular, the input light intensity splitting ratio of the MZM can be fine-tuned in response to the sign and magnitude of dispersion at various wavelengths. Notably, in the back-to-back configuration where no chromatic dispersion occurs, the BER of the 256-Gbps PAM-4 signal increases as the splitting ratio shifts from 5:5 to 1:9. This is attributed to the elevated modulation chirp and reduced ER, as shown in Supplementary Information 3. However, it is noteworthy that our adaptive chromatic dispersion compensation scheme focuses on mitigating the BER degradation encountered in practical post-fiber transmission scenarios, where chromatic dispersion varies with wavelength and distance.

### Experimental results

For a proof-of-concept demonstration, each dispersion-compensation-enabled MZM in the 4-channel transmitter is individually constructed following identical design parameters. For clarity of reference, the four MZMs in the transmitter are designated MZM-1, MZM-2, MZM-3, and MZM-4 from left to right, as illustrated in Fig. 3a. By adjusting the voltage applied to the thermal phase shifter on the  $1 \times 2$  MZI input intensity tuner, the input intensity splitting ratio of the MZM is modified, resulting in correspondingly altered static ERs, as shown in Fig. 3b. The

measured insertion loss and static ER of the MZM-1 as a function of the input intensity splitting ratio is summarized in Fig. 3c. The splitting ratio  $A^2:B^2 \approx 5:5$  when the bias voltage upon MZI intensity tuner is 1.204 V, where the maximum static ER exceeds 25 dB, with a minimum insertion loss of  $-3.6$  dB. Note that as the input light intensity imbalance between the two arms increases, the insertion loss slightly increases by  $-1$  dB, aligning with simulation results. The spectra, static ERs, and insertion losses of the other three MZMs are consistent with those of MZM-1, with each exhibiting a maximum static ER above 25 dB and a minimum insertion loss of  $-4$  dB (See Supplementary Information 5 for details). Notably, the thermal phase shifters demonstrate a maximum power consumption of only 1.98 mW for MZM input splitting ratio adjustment, as documented in Supplementary Information 4.

The EO response of the four MZMs, as characterized using a calibrated light-wave component analyzer (LCA, Keysight N5247B), is depicted in Fig. 3d. The EO bandwidth for these MZMs ranges from 28.7 GHz to 37.7 GHz at a -2 V bias voltage, with variations attributed to inadequately suppressed electrode-parasitic slotted-line modes<sup>43-45</sup>.

In order to evaluate the small-signal chirp  $\alpha$ -parameter of the MZMs, we measured the EO response of the four MZMs following 50 km standard G652.D type fiber transmission at 1271 nm, with MZM-1's result presented in Fig. 3e. According to Eq. (5), instead of modifying the splitting ratio between the two arms, the relative phase shift  $\theta_h$  between the arms was adjusted to alter the chirp's sign, facilitating streamlined device performance evaluation. The relationship between the power fading point frequency of the EO response and the MZMs' small-signal chirp  $\alpha$ -parameter is given by<sup>46</sup>:

$$f_u^2 L = \frac{c_0}{2D\lambda^2} \left[ 2 + 2u - \frac{2}{\pi} \arctan(\alpha) \right] \quad (7)$$

where  $f_u$  is the  $u$ -th order power fading point frequency of the EO response,  $L$  is the fiber length,  $c_0$  is the vacuum light speed,  $D$  is the fiber

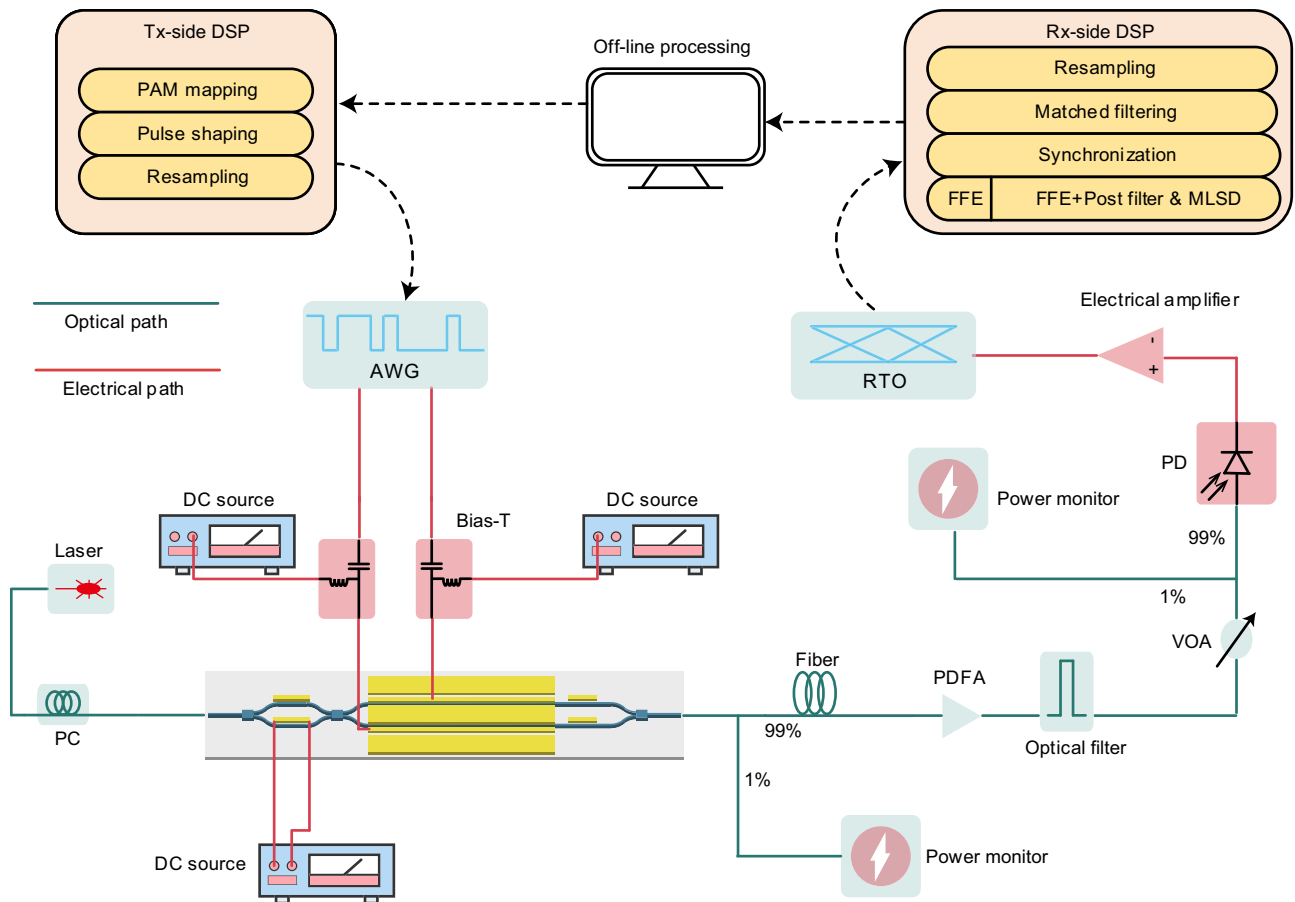


**Fig. 4 | BER measurement setup for the transmitter.** AWG arbitrary waveform generator, RTO real-time oscilloscope, PC polarization controller, PDFA Praseodymium-doped fiber amplifier, PD photodetector, FFE feed-forward equalizer, MLSD maximum likelihood sequence detection, VOA variable optical attenuator.

dispersion coefficient,  $\lambda$  is the laser wavelength, and  $\alpha$  is the chirp  $\alpha$ -parameter. The measured fiber dispersion coefficient at 1271 nm is  $-3.99$  ps/nm/km, as shown in Supplementary Information 6. As depicted in Fig. 3e, in the case where  $\theta_h = \pi/2$  ( $\theta_h = -\pi/2$ ), the first-order power fading point frequency increases (decreases) with elevated voltages applied to the thermal phase shifter of the MZI. Considering the negative fiber dispersion coefficient at 1271 nm and the relationship delineated in Eq. (7), the generated chirp of the modulated signal is positive (negative) when  $\theta_h = \pi/2$  ( $\theta_h = -\pi/2$ ). Figure 3f summarizes the extracted chirp  $\alpha$ -parameters of the MZM-1 based on the measured resonance frequency. When the bias voltage on MZI is set to 1.204 V, the chirp  $\alpha$ -parameter of MZM-1 approaches zero. Increasing the voltage results in an increment in the absolute value of the chirp  $\alpha$ -parameter. The measurement of the other three MZMs shows consistent results with a maximum  $|\alpha|$  exceeding 1, as shown in Supplementary Information 8.

The high-speed transmission performance of the transmitter was evaluated under the experimental setup illustrated in Fig. 4. The driving signal with  $\sim 2.0$  V<sub>pp</sub> peak-to-peak amplitude generated by AWG (Keysight M8199B) was mixed with a  $-2$  V DC signal using a bias-T. A continuous laser output with a power of 13 dBm is coupled to the transmitter via a fiber array, with a polarization controller (PC) employed to control the polarization of the input laser. After fiber transmission, the modulated signal is amplified (FiberLabs AMP-FL8611-0B), filtered (Santec OTF-930), attenuated, and impinging on the high-speed PD (Finisar, XPDV3320R). A broadband radio frequency amplifier (SHF M827B) amplifies the detected signal before it is fed into the real-time oscilloscope (RTO, Keysight UXR 0594B).

To refine the quality of the transmitted signal, DSP is implemented on both the transmitter and receiver. On the transmitter side, the

binary bit stream is initially mapped to a PAM-4 signal. After pulse shaping, the signal is resampled to align with the sampling rate range of the AWG and subsequently loaded to the AWG for transmission. Upon reception, the acquired signal undergoes resampling, followed by matched filtering and synchronization. Finally, the BER of the signal is calculated after applying either a feed-forward equalizer (FFE) alone or a combination of FFE and MLSD equalization to further suppress the ISI<sup>16</sup>. Specifically, FFE operates to mitigate bandwidth-induced ISI<sup>47</sup>, whereas MLSD demonstrates dual mitigation capabilities addressing both bandwidth and dispersion-induced impairments<sup>16</sup>.

The FFE employs a 155-tap finite impulse response (FIR) filter, with its coefficients adaptively updated using the recursive least squares (RLS) algorithm to achieve rapid convergence. In this study, constrained by the modulator's bandwidth limitations, we implemented FFE with increased tap counts to address bandwidth-induced ISI. Notably, employing modulators with broader bandwidths could proportionally reduce the required FFE tap configuration. The input to the FFE is a matched-filtered PAM-4 signal sampled at 2 samples per symbol (SPS). Following equalization, the signal is down-sampled to PAM-4 symbols at 1 SPS, which are subsequently used for demodulation to recover the received bits. When only FFE is employed at the receiver side, these bits and symbols are then utilized to compute the BER and signal-to-noise ratio (SNR) of the modulated signal. In the configuration incorporating both FFE and MLSD, the FFE's output signal is further filtered by a two-tap post-filter to suppress in-band noise exacerbated by the FFE in the high-frequency region<sup>48</sup>. The MLSD equalizer subsequently computes the branching metrics and employs a Viterbi algorithm-based search through the state tree structure to identify the path with the minimum cumulative branching metric,

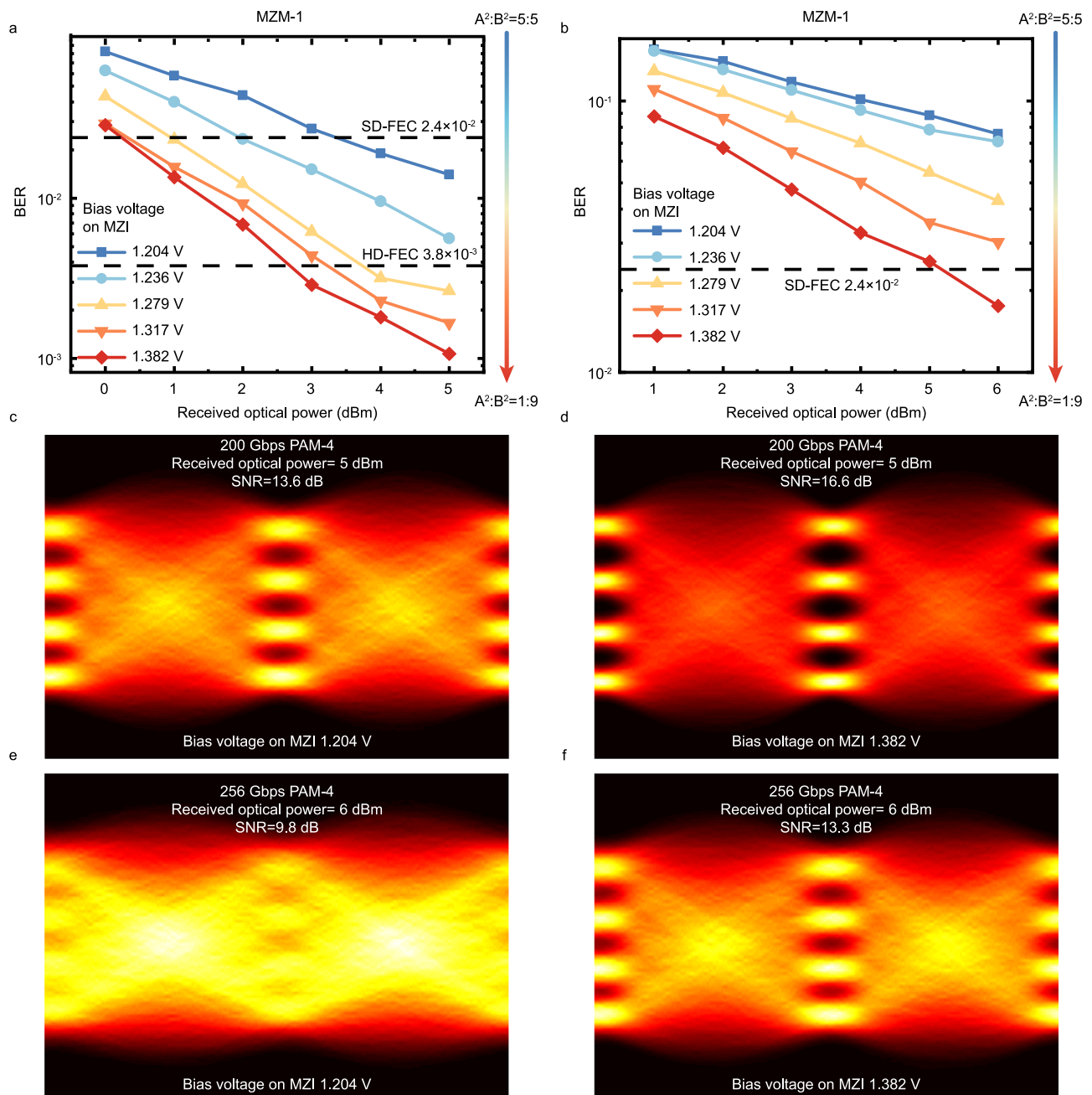


**Fig. 5 | The transmission results of MZM-1 with various bias voltages applied to the MZI tuner.** Measured BER of PAM-4 signals with (a) 200 Gbps data rate after 10 km fiber transmissions and (b) 256 Gbps data rate after 5 km fiber transmission.

c, d 200 Gbps PAM-4's eye-diagram after 10 km standard G652.D fiber transmission. e, f 256 Gbps PAM-4's eye-diagram after 5 km standard G652.D fiber transmission.

which is designated as the surviving path. Upon determining this optimal path, the system traces back through the state tree to reconstruct the most probable sequence of data signals, corresponding to the most likely transmitted PAM-4 symbols<sup>16</sup>.

In scenarios where only FFE is employed on the receiver side, the BER of MZM-1 upon 200 Gbps and 256 Gbps PAM-4 modulation after 10 km and 5 km fiber transmission is presented in Fig. 5a, b respectively. Both BER values exhibit a decreasing trend as the optical intensity difference between the MZM branches increases, highlighting the effectiveness of induced chirp in enhancing signal integrity. In the case of 200 Gbps PAM-4 modulation, with an MZI bias voltage of 1.204 V ( $A^2:B^2 \approx 5:5$ ), the BER of the MZM-1 is slightly below the SD-FEC threshold at 5 dBm received optical power after 10 km fiber transmission. Upon increased MZI bias voltage, with

consequently increased intensity splitting ratio, the BER of the MZM-1 is significantly improved to below the HD-FEC threshold, as shown in Fig. 5a. The corresponding eye diagrams of the 200 Gbps PAM-4 signal with and without optimized splitting ratio are illustrated in Fig. 5c, d. As the MZI bias voltage is optimized from 1.204 V to 1.382 V ( $A^2:B^2 \approx 1:9$ ), a 3.0 dB SNR improvement of the eye diagram is observed. In the case of 256 Gbps PAM-4 transmission, the BER at 6 dBm received optical power is below the SD-FEC threshold at 1.382 V after 5 km fiber transmission, as shown in Fig. 5b. In parallel, the quality of the eye diagrams improves significantly with a 3.5 dB increased SNR with increased MZI bias voltage, as shown in Fig. 5e, f. The progressively decreasing BER, along with sharper eye diagrams upon increased MZI bias voltage, compellingly showcases the adaptive dispersion compensation performance of the proposed scheme.

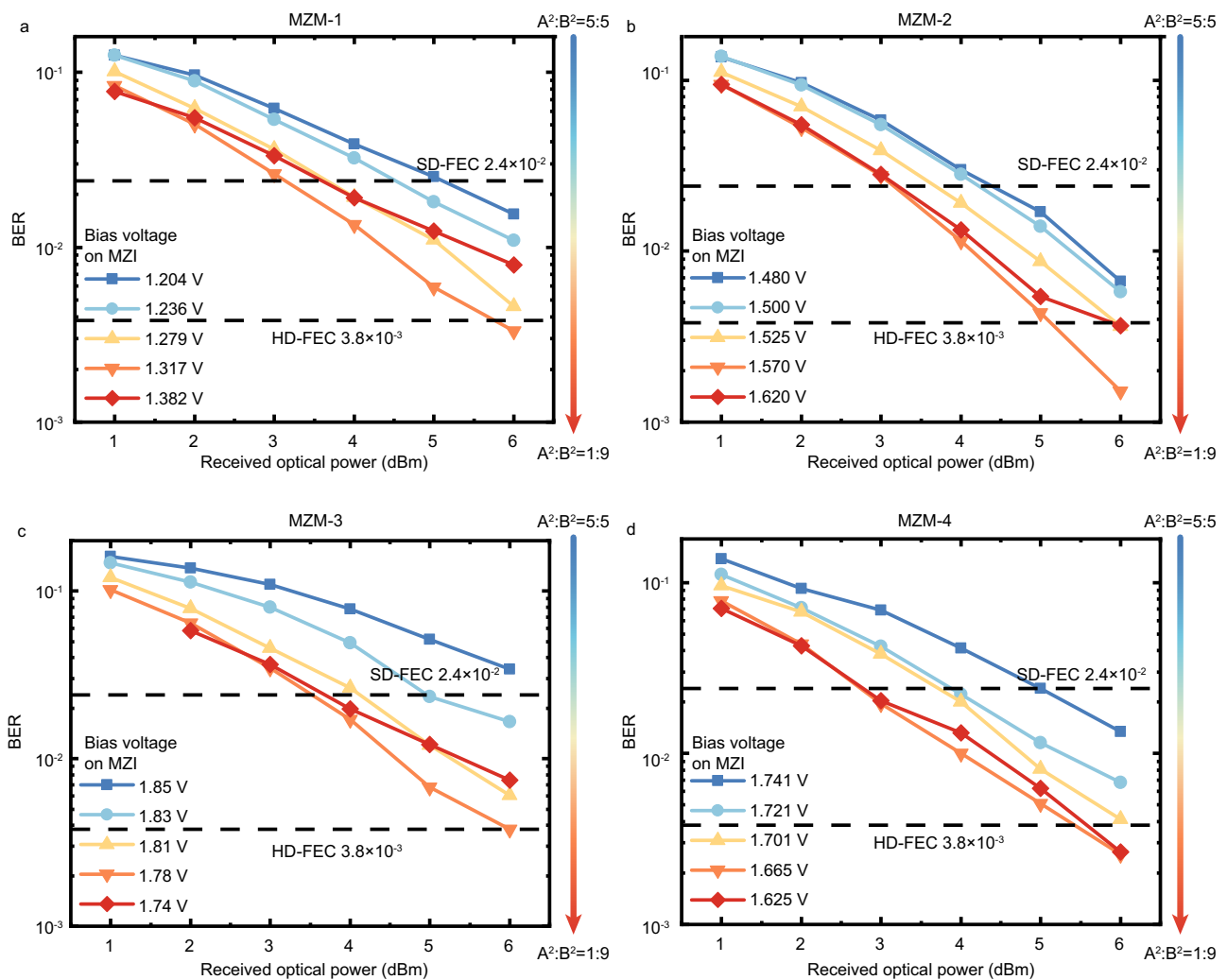


**Fig. 6 | The 256 Gbps PAM-4 transmission results of the transmitter when MLSD equalization is applied.** Measured BER of (a) MZM-1, (b) MZM-2, (c) MZM-3, and (d) MZM-4 at various bias voltages on MZI after 5 km standard G652.D fiber transmission.

The BER measurements of the other three MZMs involving 200 Gbps PAM-4 (10 km fiber) and 256 Gbps PAM-4 (5 km fiber) signals align with MZM-1's performance characteristics, as detailed in Supplementary Information 9.

In addition, we implemented the MLSD equalization approach to further suppress the ISI and thereby reduce the BER of the transmitted 256 Gbps PAM-4 signal. As shown in Fig. 6, the BERs of the four transmitting signals, with a 5 km transmission distance, are reduced to below the HD-FEC threshold. In this case, it is worth noting that since MLSD inherently provides dispersion compensation<sup>15,16,49</sup>, the BER is not minimized at 1.382 V. Instead, the BER reaches its minimum at a lower MZI bias voltage, corresponding to a reduced chirp  $\alpha$ -parameter, in light of the dispersion compensation induced by MLSD.

Notably, tuning the MZM's splitting ratio to approximately 5:5 reduces the chirp  $\alpha$ -parameter to zero, rendering the proposed transmitter functionally equivalent to a conventional unit without on-chip dispersion compensation. The consistent reduction in BER upon increased chirp  $\alpha$ -parameter across various scenarios highlights the outperformance of the proposed transmitter over non-compensated configurations.

## Discussion

The proposed adaptive dispersion-compensated silicon transmitter features silicon MZMs with an adjustable input intensity splitting ratio

tuner. By continuously adjusting the sign and magnitude of the generated chirp  $\alpha$ -parameter, this scheme enables adaptive fiber dispersion compensation across various wavelengths and fiber transmission distances in WDM applications. As shown in Table 1, in comparison with state-of-the-art high-speed O-band IM-DD fiber transmission, our work successfully achieved 5 km (10 km) fiber transmission of  $4 \times 256$  Gbps ( $4 \times 200$  Gbps) PAM-4 signals at the high-dispersion wavelength of 1271 nm. Notably, this achievement was realized without relying on power-consuming pre-emphasis at the transmitter side, while maintaining a BER below the HD-FEC threshold, marking a pioneering advancement in on-chip dispersion compensation for WDM applications. Furthermore, the proposed scheme is tailed for LAN-WDM systems operating in the 1271 nm to 1340 nm range, offering the potential for dispersion compensation of  $16 \times 256$  Gbps PAM-4 signals transmitted over extended fiber distances within the system (See Supplementary Information 10 for details).

We have demonstrated a  $4 \times 256$  Gbps silicon photonic transmitter with integrated on-chip adaptive dispersion compensation, effectively mitigating fiber chromatic dispersion in high-speed WDM systems. By utilizing MZMs with adjustable input intensity splitting ratios, our transmitter generates chirped signals with controllable magnitude and sign, enabling precise compensation of dispersion at high-dispersion wavelengths such as 1271 nm without the need for power-intensive pre-emphasis techniques. The achieved

**Table 1 | Performance comparison of the state-of-the-art high-speed O-band IM-DD transmission**

Ref	Pre-emphasis	Lane	Single-lane bit rate×Fiber length× Dispersion	FEC threshold
9	Yes	4	224 Gbps×2 km×2.1 ps/nm/km=940.8 Gbps·ps/nm	HD
10	Yes	8	250 Gbps×1 km×2.30 <sup>a</sup> ps/nm/km =575 Gbps·ps/nm 200 Gbps×10 km×2.30 <sup>a</sup> ps/nm/km =4600 Gbps·ps/nm	SD
11	Yes	1	200 Gbps×10 km×1.00 <sup>a</sup> ps/nm/km =2000 Gbps·ps/nm	SD
This work	No	4	256 Gbps×5 km×3.99 ps/nm/km =5107.2 Gbps·ps/nm 200 Gbps×10 km×3.99 ps/nm/km =7980 Gbps·ps/nm	HD

<sup>a</sup> The dispersion coefficients are derived from the wavelengths with the largest dispersion values in the corresponding work and are obtained by interpolating the maximum coefficients provided by the ITU<sup>12</sup>.

performance surpasses existing solutions that often struggle with high data rates, extended transmission distances, and energy efficiency, especially at wavelengths with significant dispersion. Moreover, the proposed scheme is applicable to LAN-WDM systems and holds the potential to support  $16 \times 256$  Gbps or  $16 \times 200$  Gbps PAM-4 signals over extended distances across standard LAN-WDM wavelengths. This work underscores the potential of silicon photonics to revolutionize optical communication technologies by enabling terabit-scale data transmission with improved energy efficiency and simplicity. By demonstrating effective on-chip adaptive dispersion compensation in high-speed WDM systems, we contribute a significant step toward meeting the escalating demands of data centers and high-performance computing systems.

## Methods

### Device fabrication and packaging

The devices were manufactured on an 8-inch commercial silicon-on-insulator (SOI) wafer featuring a 220 nm thick top silicon layer and a 3  $\mu$ m buried oxide layer, utilizing a 193 nm process node technology supplied by AMF (Singapore). The fabricated devices subsequently underwent a packaging process involving fiber array integration and DC wire bonding, performed at the SJTU-Pinghu Institute of Intelligent Optoelectronics.

### Experimental details

The spectral characteristics of the device were characterized using a lightwave measurement system (Keysight 8164B), while the current-voltage (I-V) characteristics of the thermal phase shifter were analyzed with a precision power supply (Keithley 2400). Electro-optic response measurements of the MZM were conducted via a lightwave component analyzer (Keysight N5247B), with prior calibration of the RF cable and high-speed probing system responses.

### Data availability

The data that support the findings of this study are available from the corresponding authors upon request. Source data are provided with this paper.

### Code availability

The codes that support the findings of this study are available from the corresponding authors upon request.

## References

- Kachris, C. & Tomkos, I. A Survey on Optical Interconnects for Data Centers. *IEEE Commun. Surv. Tutor.* **14**, 1021–1036 (2012).
- Thraskias, C. A. et al. Survey of Photonic and Plasmonic Interconnect Technologies for Intra-Datacenter and High-Performance Computing Communications. *IEEE Commun. Surv. Tutor.* **20**, 2758–2783 (2018).
- Shekhar, S. et al. Roadmapping the next generation of silicon photonics. *Nat. Commun.* **15**, 751 (2024).
- Wakayama, Y. et al. 400GBASE-LR4 and 400GBASE-LR8 Transmission Reach Maximization Using Bismuth-Doped Fiber Amplifiers. *J. Light Technol.* **41**, 3908–3915 (2023).
- Zhou, X., Urata, R. & Liu, H. Beyond 1 Tb/s Intra-Data Center Interconnect Technology: IM-DD OR Coherent?. *J. Light Technol.* **38**, 475–484 (2020).
- IEEE Standard for Ethernet. IEEE Std 8023-2022 (Revision of IEEE Std 8023-2018), 1-7025 (2022).
- Sector I-TTS. Characteristics of a single-mode optical fiber and cable. ITU-T Recommendations, G Series, (2016).
- Hong, Y. et al. Numerical and experimental study on the impact of chromatic dispersion on O-band direct-detection transmission. *Appl. Opt.* **60**, 4383–4390 (2021).
- Taniguchi H., Yamamoto S., Masuda A., Kisaka Y., Kanazawa S., “800-Gbps PAM-4 2-km Transmission using 4- $\lambda$  LAN-WDM TOSA with MLSE based on Deep Neural Network,” presented at the Optical Fiber Communication Conference (OFC) 2022.
- Xia, P. et al. “8×250 Gbit/s PAM4 transmission over 1 km single mode fiber with an all-silicon LAN WDM transmitter,” presented at the Optical Fiber Communication Conference (OFC) 2023.
- Li, Q. et al. Optical Amplifier-Free 100 Gbaud PAM-4 Transmission Over 10 Km SSMF Based on O-Band SiP Transceiver. *J. Light Technol.* **42**, 5175–5181 (2024).
- Bernal, S. et al. 12.1 terabit/second data center interconnects using O-band coherent transmission with QD-MLL frequency combs. *Nat. Commun.* **15**, 7741 (2024).
- Taniguchi, H. et al. “4-lambda LAN-WDM 1.6-Tb/s 2-km Transmission with Nonlinear Maximum Likelihood Sequence Estimation,” presented at the Optical Fiber Communication Conference (OFC) 2024.
- Juarez A. A., Zhu Y., Chen X., Li M.-J. Design Considerations for 1.6 Tbit/s Data Center Interconnects: Evaluating IM/DD and Coherent Transmission over O-Band Transmission Window. *Photonics* **11**, (2024).
- Nagarajan, R. et al. Recent Advances in Low-Power Digital Signal Processing Technologies for Data Center Applications. *J. Light Technol.* **42**, 4222–4232 (2024).
- Zhu, Y. et al. Toward Single Lane 200G Optical Interconnects With Silicon Photonic Modulator. *J. Light Technol.* **38**, 67–74 (2020).
- Johnson J. Chirp characteristics and chromatic dispersion tolerance of 200 G EML transmitters. IEEE 8023 df 200 Gb/s-16 Tb/s Ethernet Task Force, (2022).
- Zhu, B. et al. C-band 312Gbps PAM8 Transmission Over 30km SMF Using Integrated Optical Dispersion Compensator. *J. Light Technol.* **1-7** (2024).
- Tao, M. et al. “Improved Dispersion Tolerance for 50G-PON Downstream Transmission via Receiver-Side Equalization,” presented at the Optical Fiber Communication Conference (OFC) 2019.
- Nagarajan, R., Lyubomirsky, I. & Agazzi, O. Low Power DSP-Based Transceivers for Data Center Optical Fiber Communications (Invited Tutorial). *J. Light Technol.* **39**, 5221–5231 (2021).
- Chen G. F. R., Ong K. Y. K., Tan D. T. H. Chip-Scale Dispersion Compensation of High-Speed Data – Recent Progress and Future Perspectives. *Laser & Photonics Reviews*, (2024).
- Morero, D. A., Castrillon, M. A., Aguirre, A., Hueda, M. R. & Agazzi, O. E. Design Tradeoffs and Challenges in Practical Coherent Optical Transceiver Implementations. *J. Light Technol.* **34**, 121–136 (2016).

23. Pfaff, D. et al. A 224 Gb/s 3 pJ/bit 40 dB Insertion Loss Transceiver in 3-nm FinFET CMOS. *IEEE J. Solid-State Circuits* **60**, 9–22 (2025).
24. Mostafa, A. et al. “7.2: A 2.2pJ/b 212.5Gb/s PAM-4 Transceiver with 46dB Reach in 5nm FinFET,” presented at the 2025 IEEE International Solid-State Circuits Conference (ISSCC).
25. Omirzakhov K., Hao H., Pirmoradi A., Aflatouni F. Energy Efficient Monolithically Integrated 256 Gb/s Optical Transmitter With Autonomous Wavelength Stabilization in 45 nm CMOS SOI. *IEEE Journal of Solid-State Circuits*, 1-10 (2024).
26. Siew, S. Y. et al. Review of Silicon Photonics Technology and Platform Development. *J Light Technol*, 1-1 (2021).
27. Sia, J. X. B. et al. Wafer-Scale Demonstration of Low-Loss (similar to 0.43 dB/cm), High-Bandwidth (> 38 GHz), Silicon Photonics Platform Operating at the C-Band. *Ieee Photonics J.* **14**, 1–1 (2022).
28. Moreira R., Gundavarapu S., Blumenthal D. J. Programmable eye-opener lattice filter for multi-channel dispersion compensation using an integrated compact low-loss silicon nitride platform. *Opt Express* **24**, (2016).
29. Brodnik G. M., Pinho C., Chang F., Blumenthal D. J., “Extended Reach 40km Transmission of C-Band Real-Time 53.125 Gbps PAM-4 Enabled with a Photonic Integrated Tunable Lattice Filter Dispersion Compensator,” presented at the Optical Fiber Communication Conference.
30. Giuntoni, I. et al. Continuously tunable delay line based on SOI tapered Bragg gratings. *Opt Express* **20**, (2012).
31. Liu S., He J., Dai D., “Tunable Dispersion Compensator Based on Taper Bragg Gratings with Heating-Engineering,” presented at the Asia Communications and Photonics Conference 2021.
32. Liu, S. et al. On-Chip Circulator-Free Chirped Spiral Multimode Waveguide Grating for Dispersion Management. *ACS Photonics* **10**, 1654–1661 (2023).
33. Liu, Y. et al. “Silicon Integrated Continuously Tunable Dispersion Compensator Based on Cascaded Micro-Ring Resonators,” presented at the Asia Communications and Photonics Conference (ACP) 2022.
34. Liu, Y. et al. Parallel wavelength-division-multiplexed signal transmission and dispersion compensation enabled by soliton micro-combs and microrings. *Nat. Commun.* **15**, 3645 (2024).
35. Forward error correction for high bit-rate DWDM submarine systems.) (2004).
36. Che, D. & Chen, X. Modulation Format and Digital Signal Processing for IM-DD Optics at Post-200G Era. *J. Light Technol.* **42**, 588–605 (2024).
37. Wenke, G. & Klimmek, M. Considerations on the  $\alpha$ -factor of non-ideal, external optical Mach-Zehnder modulators. *J. optical Commun.* **17**, 42–48 (1996).
38. Wang, Z., Gao, Y., Kashi, A. S., Cartledge, J. C. & Knights, A. P. Silicon Microring Modulator for Dispersion Uncompensated Transmission Applications. *J. Light Technol.* **34**, 3675–3681 (2016).
39. Wu, X., Guan, B., Xu, Q., Doerr, C. & Chen, L. Low-chirp push-pull dual-ring modulator with 144 Gb/s PAM-4 data transmission. *Opt. Express* **28**, 26492–26498 (2020).
40. Li, R. et al. High-speed low-chirp PAM-4 transmission based on push-pull silicon photonic microring modulators. *Opt. Express* **25**, 13222–13229 (2017).
41. He, J. et al. Twelve-channel LAN wavelength-division multiplexer on lithium niobate. *Nanophotonics* **13**, 85–93 (2024).
42. Union I. T. Characteristics of a single-mode optical fibre and cable.) (2016).
43. Tu, X. et al. Silicon optical modulator with shield coplanar waveguide electrodes. *Opt. Express* **22**, 23724 (2014).
44. Hao, X. et al. Demonstration and Characterization of High-Speed Silicon Depletion-Mode Mach-Zehnder Modulators. *IEEE J. Sel. Top. Quantum Electron.* **20**, 23–32 (2014).
45. Dong, P., Sinsky, J. H. & Gui, C. Coplanar-waveguide-based silicon Mach-Zehnder modulator using a meandering optical waveguide and alternating-side PN junction loading. *Opt. Lett.* **41**, 4401–4404 (2016).
46. Devaux, F., Sorel, Y. & Kerdiles, J. F. Simple measurement of fiber dispersion and of chirp parameter of intensity modulated light emitter. *J. Light Technol.* **11**, 1937–1940 (1993).
47. Li, D. et al. Low-complexity equalization scheme for suppressing FFE-enhanced in-band noise and ISI in 100 Gbps PAM4 optical IMDD system. *Opt. Lett.* **45**, 2555–2558 (2020).
48. Yu, Y., Che, Y., Bo, T., Kim, D. & Kim, H. Reduced-state MLSE for an IM/DD system using PAM modulation. *Opt. Express* **28**, 38505–38515 (2020).
49. Jacques, M. et al. 240 Gbit/s Silicon Photonic Mach-Zehnder Modulator Enabled by Two 2.3-Vpp Drivers. *J. Light Technol.* **38**, 1–1 (2020).

## Acknowledgements

Y. Li acknowledges the funding from the National Natural Science Foundation of China (NSFC) under Grant 62305212.

## Author contributions

S.R. simulated, designed, and measured the device. Yu.G. collaborated on the high-speed transmission tests and conducted the offline DSP. Y. Liu, T.M., Y.W., Y.Q., Yuyao.G.,L.L., Y.Z., Q.Z., J.C., and L.Z. helped analyze the data. S.R., Y.Li., and L.Z. prepared the manuscript.

## Competing interests

The authors declare no competing interests.

## Additional information

**Supplementary information** The online version contains supplementary material available at <https://doi.org/10.1038/s41467-025-61408-7>.

**Correspondence** and requests for materials should be addressed to Yu Li or Qunbi Zhuge.

**Peer review information** *Nature Communications* thanks the anonymous reviewers for their contribution to the peer review of this work. A peer review file is available.

**Reprints and permissions information** is available at <http://www.nature.com/reprints>

**Publisher's note** Springer Nature remains neutral with regard to jurisdictional claims in published maps and institutional affiliations.

**Open Access** This article is licensed under a Creative Commons Attribution-NonCommercial-NoDerivatives 4.0 International License, which permits any non-commercial use, sharing, distribution and reproduction in any medium or format, as long as you give appropriate credit to the original author(s) and the source, provide a link to the Creative Commons licence, and indicate if you modified the licensed material. You do not have permission under this licence to share adapted material derived from this article or parts of it. The images or other third party material in this article are included in the article's Creative Commons licence, unless indicated otherwise in a credit line to the material. If material is not included in the article's Creative Commons licence and your intended use is not permitted by statutory regulation or exceeds the permitted use, you will need to obtain permission directly from the copyright holder. To view a copy of this licence, visit <http://creativecommons.org/licenses/by-nc-nd/4.0/>.

© The Author(s) 2025, corrected publication 2025